crystals

MDPI

Article

A Dual-Criterion System for Surface-Localized States Identification: Application to Al(001) Surface

Xihui Liang [1,*] and Dah-An Luh [2,3,*]

[1] School of Arts and Sciences, Guangzhou Maritime University, Guangzhou 510725, China
[2] Department of Physics, National Central University, Taoyuan 320317, Taiwan
[3] National Synchrotron Radiation Research Center, Hsinchu 300092, Taiwan
* Correspondence: liangxihui@gzmtu.edu.cn (X.L.); luh.dah.an@gmail.com (D.-A.L.)

Abstract

Angle-resolved photoemission spectroscopy (ARPES) clearly resolves surface-localized (SL) states, yet conventional density functional theory (DFT) band structures from slab calculations do not readily distinguish weakly confined SL states on surfaces such as Al(001), as traditional layer-threshold criteria fail for surfaces with long surface-state decay lengths. We establish a dual-criterion scheme using the surface ratio R and the localization integral L weighted by the inelastic mean free path (IMFP) to quantitatively distinguish SL states: R quantifies the surface-projected charge fraction, while L incorporates the photoelectron IMFP to mimic ARPES surface sensitivity, both evaluated within a fully converged 81-layer Al(001) slab that eliminates artificial inter-surface coupling. Band structures color-coded by R and L intuitively highlight SL states as bright yellow-white bands against red bulk backgrounds. Our calculations show that continuum SL features arise from multi-band hybridization (sharp surface resonances). Notably, R and L alone cannot separate absolute surface states from resonances. All DFT calculations were performed using the PBEsol exchange-correlation functional within the GGA framework, the PAW formalism, and an 81-layer Al(001) slab model. This work reveals the electronic nature of surface features on Al(001) and provides a quantitative SL-state identification tool that is conceptually transferable to other crystalline surfaces.

Keywords: surface-localized states; dual-criterion system; Al(001); ARPES; DFT; IMFP

1. Introduction

Surface-localized (SL) electronic states are eigenstates spatially confined near the surface due to the abrupt termination of the crystalline periodic potential. Their wavefunctions decay exponentially (or quasi-exponentially) along the surface normal and are predominantly concentrated within the outermost few atomic layers. The accurate identification of SL states is essential for understanding a wide range of surface-related phenomena, from photoemission spectroscopy to topological electronic states [1–6]. Angle-resolved photoemission spectroscopy (ARPES) is arguably the most powerful experimental technique for identifying such SL states on crystalline surfaces, such as those of topological insulators, superconductors, two-dimensional materials, and metals [7–20]. SL states typically appear as distinct, well-resolved spectral peaks in ARPES and can thus be readily separated from the featureless bulk continuum, regardless of whether they lie within absolute band gaps or symmetry gaps in the projected bulk shadow region [7–14,21–25].

Academic Editor: Thomas M. Klapötke

Received: 1 July 2026
Revised: 4 August 2026
Accepted: 11 August 2026
Published: 13 August 2026

Meanwhile, density functional theory (DFT) has been extensively applied to investigate the electronic, magnetic, thermoelectric, and structural properties of a wide range of bulk materials, including Heusler alloys [26,27] and rare-earth intermetallic compounds [28]. In parallel, ab initio molecular dynamics (AIMD) simulations have provided complementary insights into surface-related atomistic processes in Al-containing systems at finite temperatures [29]. These diverse DFT-based approaches have greatly advanced our understanding of materials properties from bulk thermodynamics to surface chemistry [30–35]. However, when it comes to the specific task of identifying surface-localized electronic states from slab band structures, conventional slab-based DFT band structures suffer from a fundamental limitation: surface and bulk eigenstates are densely interwoven across the entire energy-momentum space, with no intrinsic criterion to automatically identify SL-state features. Early theoretical studies have proposed various criteria for identifying SL states in slab model calculations, primarily based on the spatial localization of wavefunction probability density, charge density, or amplitude within the outermost two atomic layers. For instance, Kern and Hafner required over 70% intensity within the first two layers of diamond (110) [36], while Gay et al. imposed an 80% probability-density threshold for Cu(100) [37]. Takeuchi et al. and Bullett adopted a more moderate 50% amplitude criterion for Au(100) and W(001), respectively [38,39]. However, these established criteria were primarily tailored for strongly or moderately confined surface states with a clear energy gap separating them from bulk states. Their applicability becomes questionable for surface states with weaker confinement. A prototypical case is Al(001), whose surface states display weak localization and an exceptionally long decay depth compared to other *fcc* metal surfaces [40,41]. For instance, the Al(001) surface state at the $\overline{\Gamma}$ point has a decay depth of ~12 Å, which is five times that of the Cu(100) surface state at the $\overline{\Gamma}$ point [41]. Furthermore, Al(001) surface states feature a much lower fraction of their probability density localized within the outermost two atomic layers—falling well below even the most lenient 50% threshold. Consequently, the quantitative layer-localization criteria confined to the topmost two or three atomic layers from earlier studies become inapplicable. For example, the surface state residing in the narrow *sp* band gap along the $\overline{\Gamma} - \overline{X}$ path was not identified by two earlier studies [42,43].

This inconsistency across localization criteria—both in the number of layers sampled and the required localization percentage—leads to ambiguous identification of SL states, depending on the chosen definition. This ambiguity also hinders direct and quantitative alignment between first-principles band structures and experimental ARPES dispersions, making it difficult to reliably reproduce or predict the SL-state features measured in photoemission experiments.

Given these challenges, there is a clear need for a robust and precise identification methodology for SL states. Taking the Al(001) surface as a prototypical metal surface model, this work develops a complete DFT-based identification scheme. Our goal is to reproduce the clear, ARPES-like discrimination of SL states from bulk bands in computed band structures.

2. Materials and Methods

All first-principles calculations were performed using the Quantum ESPRESSO software package (Version: 7.5) [44,45], based on DFT and the plane-wave pseudopotential method. The revised Perdew-Burke-Ernzerhof for solids (PBEsol) exchange-correlation functional within the generalized gradient approximation (GGA) was adopted to describe electron-electron interactions [46]. The projector augmented-wave (PAW) formalism, obtained from the Standard Solid-State Pseudopotential (SSSP) library optimized for precision (version 1.3.0) [47,48], was used for electron-ion interactions, with Al 3*s* and 3*p* electrons

treated as valence electrons. We selected the PBEsol functional because it delivers more accurate lattice parameters for bulk solids than PBE, yielding an equilibrium lattice constant in close agreement with experiment—critical for reliable surface electronic structure predictions [49]. The PAW method with a plane-wave basis, using the SSSP library, is a well-benchmarked and widely used approach that provides high accuracy for both total energies and wavefunctions while being computationally efficient for large supercells [47,48].

An 81-layer Al(001) slab model was adopted in this work, whose convergence was verified by the negligible energy splitting (<1.0 meV at the $\overline{\Gamma}$ point) between the two surface states originating from the top and bottom surfaces of the slab. The slab was constructed based on the bulk aluminum crystal structure (optimized lattice constant: 4.02 Å, obtained from structural optimization of bulk aluminum, consistent with experimental lattice data) [49], with a 15-Å vacuum region added on both sides to eliminate artificial inter-slab electronic coupling. The central 59 atomic layers were fixed during structural relaxation to mimic the bulk aluminum lattice geometry, while the outermost 11 layers on both sides of the slab were symmetrically relaxed until the residual force on each relaxed atom was less than 0.01 eV/Å. Only the outermost 11 atomic layers were relaxed, since Sferco et al. verified that the 12th layer and beyond exhibit negligible lattice relaxation. These inner layers were therefore fixed at their bulk positions without loss of accuracy for surface property calculations [50].

Systematic convergence tests were carried out on slabs with 31, 41, 51, 61, 71, and 81 atomic layers. The surface-state energy splitting at the $\overline{\Gamma}$ point was used as the convergence metric. Slabs thinner than 61 layers exhibit energy splitting exceeding 10 meV, while the 81-layer slab suppresses this splitting below 1.0 meV. Full convergence data are compiled in Supplementary Table S1, confirming that the 81-layer slab provides adequate thickness for surface electronic structure simulations.

The self-consistent field (SCF) convergence threshold was set to 1×10^{-8} eV. A plane-wave cutoff energy of 450 eV and a charge density cutoff energy of 1800 eV were employed, combined with a $22 \times 22 \times 1$ Monkhorst-Pack k-point grid for Brillouin zone sampling. Marzari-Vanderbilt cold smearing with a broadening of 0.001 eV and a local Thomas−Fermi mixing mode were used to accelerate total energy convergence [51]. The vacuum region thickness, plane-wave cutoff energy, charge density cutoff energy, k-point sampling for Brillouin zone integration, and smearing width were all determined via systematic convergence tests, with a total energy convergence criterion of 1 meV/atom.

Notably, for the 81-layer Al(001) slab model employed in our calculations, the surface-state energy splitting at the $\overline{\Gamma}$ point originating from inter-surface coupling is fully converged, with a splitting magnitude below 1.0 meV. Thinner slabs (5–30 layers) show inadequate convergence, as the long decay length of the surface states leads to significant wavefunction overlap between the two surfaces. This electronic coupling causes non-negligible energy splitting and distorts the wavefunction decay behavior. The 81-layer slab satisfies convergence requirements for both surface wavefunction decay depth and inter-surface decoupling, ensuring that calculated wavefunction distributions reflect intrinsic Al(001) surface electronic properties free from slab-thickness-induced artificial effects.

Orbital-projected band analysis was performed using the projwfc.x post-processing tool of Quantum ESPRESSO to decompose the electronic states into contributions from orthogonalized atomic orbitals (e.g., p_z, and p_x/p_y). This decomposition reveals the orbital character responsible for the localization asymmetry observed across distinct surface states.

The wavefunction probability density distribution $|\psi(z)|^2$ (z-axis perpendicular to the slab surface plane) was extracted using the pp.x post-processing module embedded in Quantum ESPRESSO, and quantitatively processed by customized Python 3.12.3 scripts. Specifically, pp.x outputs three-dimensional (3D) charge density data in the standard cube

file format; homemade Python codes parsed cube files, reconstructed density arrays, and integrated 3D charge density over in-plane x and y directions to obtain one-dimensional density profiles along the z direction.

Atomic structure manipulations were carried out using the Atomic Simulation Environment (version 3.25.0) [52]. All band and profile figures were plotted using Veusz (version 4.1) [53].

3. Results

3.1. Wavefunction Probability Density Distribution of SL and Bulk States

Figure 1a shows the band structure of the 81-layer Al(001) slab along the $\overline{\mathrm{M}}-\overline{\Gamma}-\overline{\mathrm{X}}$ high-symmetry line in the two-dimensional Brillouin zone, with energy referenced to the Fermi level (E_F = 0 eV). The well-documented $\overline{\Gamma}$ surface state band (S_1), with its minimum located at approximately -2.8 eV at the $\overline{\Gamma}$ point, resides within the large projected bulk band gap and can be identified straightforwardly. The $\overline{\mathrm{X}}$ surface state band (S_2) reaches its minimum of approximately -4.6 eV at the $\overline{\mathrm{X}}$ point, confined within the narrow *sp*-derived band gap and lying close to the lower edge of the gap. A parabolic feature in the region marked W_1 (enclosed by a red closed arc-shaped outline) has a band minimum of -0.82 eV and comprises connected band segments, exhibiting free-electron dispersion. By contrast, the regions labeled W_2 (enclosed by a green box) and W_3 (enclosed by a blue box) do not exhibit distinguishable SL-state bands in conventional band plots. Nevertheless, high-resolution ARPES measurements revealed continuous bright features within these three regions, which match typical surface-state spectroscopic characteristics [24,25]. This discrepancy highlights the limitation of conventional DFT band analysis: surface-derived features overlapped with projected bulk states cannot be recognized intuitively, unlike clear ARPES spectral signals.

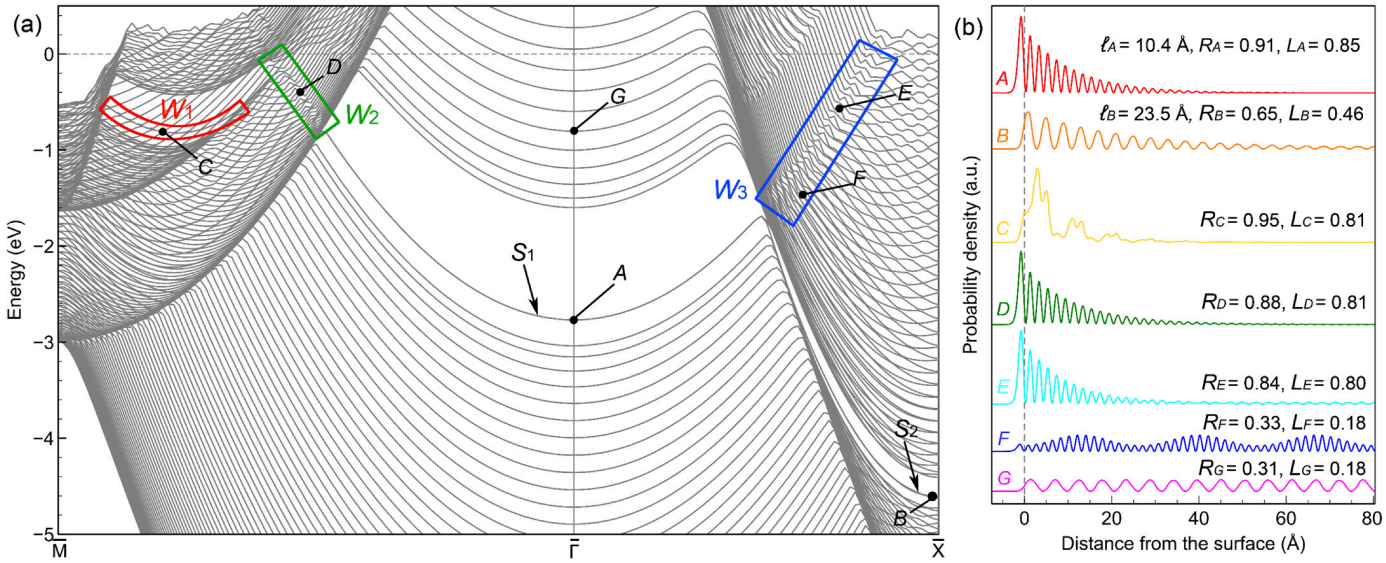

Figure 1. (**a**) Band structure of the 81-layer Al(001) slab along the $\overline{\mathrm{M}}-\overline{\Gamma}-\overline{\mathrm{X}}$ high-symmetry line in the two-dimensional Brillouin zone. Energy is referenced to the Fermi level (E_F = 0 eV). (**b**) Out-of-plane wavefunction probability density profiles of representative states *A*–*G* labeled in panel (**a**). The fitted decay depth (ℓ) of states *A* and *B*, the surface ratio (R) and the localization integral (L) of all these states are appended beside the corresponding curves. Only density profiles of the upper slab half are plotted for clarity, owing to the centrosymmetric wavefunction distribution of the symmetric slab model.

As demonstrated in subsequent sections, the features within the W_1–W_3 regions—though overlapped and obscured by bulk states in raw band plots—can be reliably identified as SL states via the proposed dual-criterion system.

Figure 1b presents out-of-plane wavefunction probability density profiles of several representative states (*A*–*G*) marked in Figure 1a. Here, z = 0 Å corresponds to the topmost slab surface, and z = 80.37 Å marks the slab's central mirror plane. The symmetric Al(001) slab possesses central inversion symmetry along the z-axis, leading to a centrosymmetric wavefunction probability density distribution relative to the slab center. For visualization clarity, only the density profiles of the upper half of the slab are shown.

State *A* exhibits a dominant density peak at ~0.8 Å, decaying steeply to ~0.01% of the maximum amplitude at ~5.0 Å outside the top surface in vacuum. By comparison, state *B* reaches its primary density peak at ~0.8 Å inside the outermost surface layer. Both states show gradual amplitude attenuation propagating toward inner bulk layers, featuring the characteristic long decay depth of Al(001) SL states, which validates the necessity of a thick slab to eliminate bilateral surface electronic interference.

State *C* shows irregular successive density oscillations along the z direction with decreasing peak amplitude. Such non-monotonic decay originates from electronic hybridization between surface-originated states and bulk Bloch states. Even so, state *C* is highly surface-localized, owing to its very high density near the surface and negligible density in the bulk.

States *D* and *E* share similar surface-peaked density profiles to the typical SL state *A*, while the peak height of state *E* decays monotonically until ~20 Å. This indicates bulk-state mixing effects.

In stark contrast to SL states, bulk states *F* and *G* exhibit two distinct density profiles. State *F* displays sharp, comb-like peaks with a periodically modulated envelope throughout the slab. State *G* exhibits wider-spaced, cosine-like undulations with no obvious envelope modulation. Neither state presents enhanced charge density near the surface, confirming intrinsic bulk electronic characteristics.

The peak-height envelopes of the surface states *A* and *B* were fitted to exponential decay functions: $n_{\text{envelope}} = a_0 e^{-\frac{z}{\ell}}$, where ℓ is the decay depth and a_0 is the maximum surface probability density. The fitted decay depth is 10.4 Å for state *A* (at $\overline{\Gamma}$) and 23.5 Å for state *B* (at $\overline{\text{X}}$). The decay depth of state *A* is slightly smaller than the 12 Å value reported by Knebl [41]; this discrepancy likely arises from differences in slab geometries. The 81-layer slab adopted in this work has a 59-layer bulk core and fully relaxed bilateral outer layers, achieving complete inter-surface decoupling. The thinner 25-layer slab used in previous work fails to realize full decoupling, resulting in an overestimated surface decay depth.

3.2. Dual-Criterion System for Surface State Identification

A dual-criterion system based on out-of-plane wavefunction probability density distribution was established to distinguish SL states from bulk states, defined as follows:

3.2.1. Surface Ratio Criterion

The surface ratio criterion (R) is defined as the ratio of integrated wavefunction probability density within the defined surface region to the total integrated density over the entire slab. The surface region covers the outermost n atomic layers plus a 5-Å vacuum region above the surface. The value of n is determined by the maximum fitted decay depth of surface states at high-symmetry points. For Al(001), we set n = 12, which corresponds to approximately 23.5 Å, the decay depth of surface state *B* at the $\overline{\text{X}}$ point.

The calculation formula for R is:

$$R = \frac{\int_{\text{surface region}} |\psi(z)|^2 dz}{\int_{\text{entire slab}} |\psi(z)|^2 dz}. \quad (1)$$

3.2.2. Localization Integral Criterion

The second criterion is the localization integral criterion (L), defined as:

$$L = \int |\psi(z)|^2 e^{-\frac{z}{\lambda}} dz, \quad (2)$$

where $z = 0$ at the top surface and λ is the inelastic mean free path (IMFP) of electrons in aluminum. Here, $\lambda = 3.17$ Å is taken from the NIST Electron Inelastic Mean Free Path Database (Version 1.2) [54]. This IMFP value corresponds to a photoelectron kinetic energy of approximately 50 eV, matching the effective probe energy of the ARPES experiments by Liang et al. [24]. The exponential weight $e^{-\frac{z}{\lambda}}$ enhances the contribution of the surface region while suppressing the bulk contribution, consistent with the surface-sensitive detection mechanism of ARPES.

Considering the centrosymmetric wavefunction probability density of the symmetric slab, only density data of the upper slab half were calculated to improve computational efficiency. The 5-Å outer vacuum region is included in the integration, because of the density distribution behavior of the $\overline{\Gamma}$ surface state (state A) shown in the previous section. Omitting this low-amplitude density tail would drastically underestimate the intrinsic localization strength of SL states.

3.3. Identification of SL States Using the Dual-Criterion System

The R and L values of all states on the computed Al(001) band structure were systematically calculated, and statistical value distributions are presented as histograms in Figure 2a,b, respectively. The R and L values of representative states A–G are marked in Figure 1b. Notably, SL states located either inside absolute band gaps ($R = 0.91$, $L = 0.85$ for state A) or within the projected bulk continuum ($R = 0.88$, $L = 0.81$ for state D) possess far higher R and L values than typical bulk states ($R = 0.31$, $L = 0.18$ for state G).

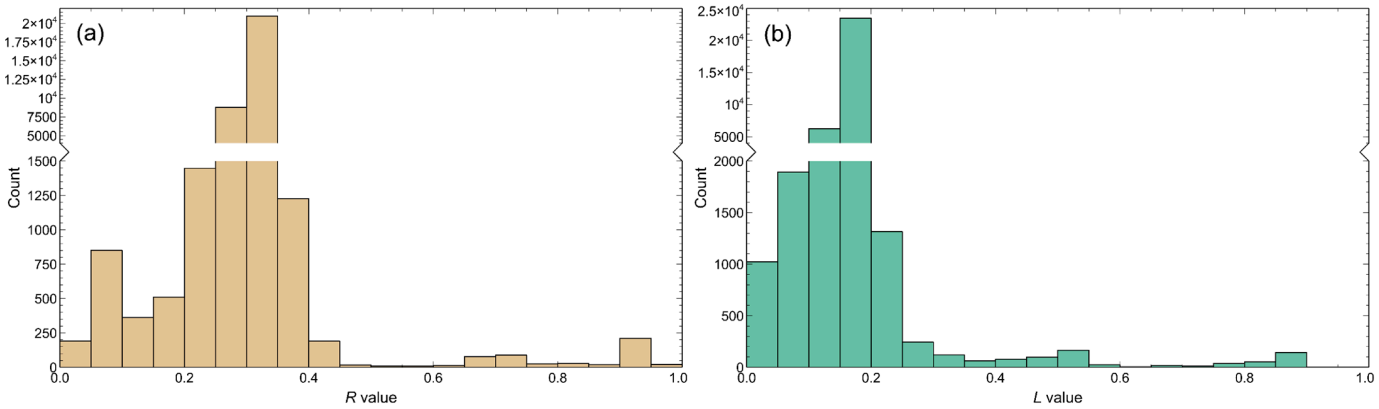

Figure 2. Statistical histograms of the calculated (**a**) surface ratio R and (**b**) localization integral L. The vertical count axis is broken to improve visualization of low-count bins.

As shown in Figure 2a, most states cluster at $R = 0.0$–0.5, forming a dominant bulk-state population, while a minor high-value subset spanning 0.6–1.0 corresponds exclusively to SL states. Similarly, in Figure 2b, bulk states concentrate at $L = 0$–0.25, whereas SL states form an isolated high-L-value cluster ranging from 0.65 to 0.90. This distinct numerical

gap enables unambiguous binary discrimination between SL states and bulk states via the dual-threshold criterion.

The band structures color-coded by the R and L values are presented in Figure 3a,b, respectively. It is evident that the red bands represent bulk states with low R and L values, whereas the yellow bands correspond to SL states with high R and L values. Since the majority of states appear in red, the minority yellow states stand out clearly, achieving ARPES-equivalent intuitive identification effects and enabling straightforward identification of the SL-state features.

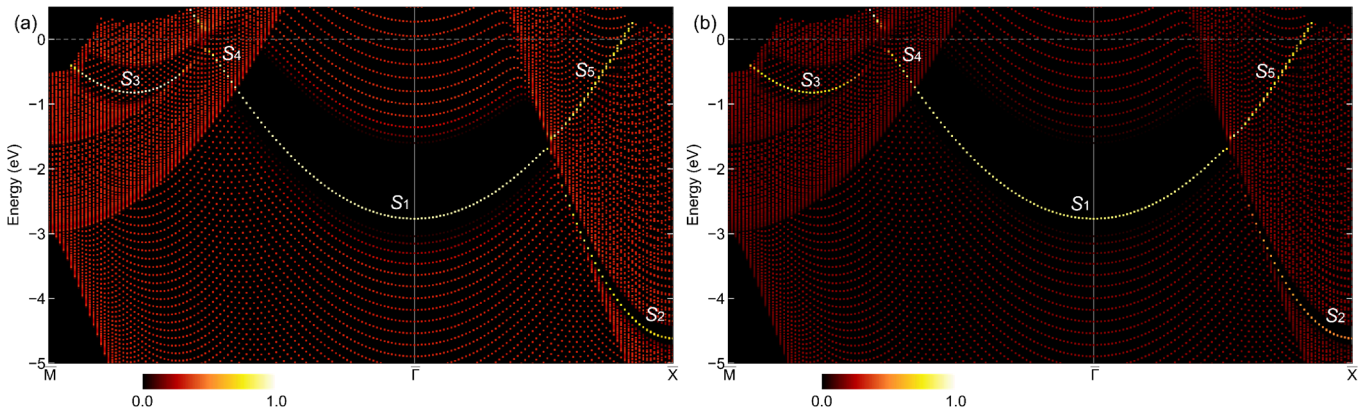

Figure 3. Band structures color-coded by (**a**) the surface ratio R and (**b**) the localization integral L with a heatmap scale ranging from 0.0 (black) to 1.0 (white). In both panels, high numerical values (yellow-white coloration) denote SL states, while low values (red) denote bulk states against a black background. Energy is referenced to the Fermi level ($E_F = 0$).

The highlighted S_1–S_5 SL states in Figure 3a,b exhibit striking similarity in both position and shape to previous high-resolution ARPES spectra and earlier theoretical calculations [24,55,56]. Notably, the correspondence between our calculated SL-state features and the ARPES bands reported by Liang et al. is summarized as follows: our S_2 and S_3 dispersions align perfectly with their experimental S_2 and S_3 signals, respectively, whereas our S_4 and S_1 collectively correspond to the long continuous segment of their S_1 feature, spanning from around the middle of $\overline{\mathrm{M}} - \overline{\Gamma}$ through $\overline{\Gamma}$ to the avoided-crossing region around the middle of $\overline{\Gamma} - \overline{\mathrm{X}}$. Beyond this crossing, our S_5 resembles the remaining segment of their S_1 feature [24].

A comparison of the minimum energy positions below the Fermi level and the effective masses of the S_1, S_2, and S_3 features with previous experimental and calculated values is summarized in Table 1. The small discrepancy arises from the combined error ranges of DFT calculations and ARPES experiments, as well as the limited slab thickness in other theoretical studies.

Table 1. Comparison of the SL-state features (S_1–S_3) of Al(001) with previous experiments and other theoretical calculations. E_{min} stands for the minimum energy position below the Fermi level. m_{eff} is the effective mass. m_e is the rest mass of a free electron.

SL States	Parameters	This Paper	Previous Experiments	Other Calculations
S_1	E_{min}	2.77 eV	2.75 eV [25,57] 2.80 eV [24]	2.67 eV [55] 2.81 eV [58]
	m_{eff}	1.07 m_e	1.03 m_e [59], 1.07 m_e [24]	1.09 m_e [41] 1.11 m_e [42]

Table 1. *Cont.*

SL States	Parameters	This Paper	Previous Experiments	Other Calculations
S_2	E_{min}	4.61 eV	4.55 eV [57] 4.62 eV [24]	4.55 eV [42] 4.63 eV [58]
	m_{eff}	0.36 m_e	0.35 m_e [24]	N.A.
S_3	E_{min}	0.82 eV	0.82 eV [24]	N.A.
	m_{eff}	0.57 m_e	0.52 m_e [24]	N.A.

Notes: N.A. = not available.

4. Discussion

4.1. Classification of SL States: Absolute, Relative, and Resonances

Based on energy position, the SL states identified by our dual-criterion system fall into two categories: those inside projected band gaps and those within the projected bulk continuum. Three classification schemes have been proposed in the literature. Heinrichsmeier and many other researchers distinguished intrinsic surface states (inside band gaps) from surface resonances (inside bulk continuum) solely by energy position [25,42,60]. Wachutka defined relative surface states as symmetry-protected bound states within the continuum, where hybridization is forbidden—distinct from absolute surface states that reside in absolute band gaps [56]. Hummel and Bross adopted a practical classification based on numerical sharpness, categorizing continuum hybridized states as surface resonances and grading them by sharpness [55].

Our analysis reveals a fundamental difference between gap states and continuum states. Within the absolute band gaps, a single continuous band (e.g., S_1) maintains dominant surface character throughout the $k_{||}$ range of the gaps. By contrast, within the projected bulk continuum (e.g., S_3), no single band sustains dominant surface character across multiple $k_{||}$ points; instead, this character shifts between different bands at different $k_{||}$ values—a behavior we term the "band-to-band relay" phenomenon. This phenomenon originates from inevitable hybridization between surface-originated wavefunctions and bulk Bloch states, which disperses surface character over multiple hybrid states and prevents the formation of single continuous surface bands. Consequently, these continuum-distributed SL features should be categorized as sharp surface resonances rather than ideal relative surface states.

To our knowledge, previous theoretical studies of Al(001) surface electronic properties did not report this "band-to-band relay" phenomenon. In a finite-thickness slab, the quantization of k_z generates a set of discrete hybridized bands at each sampled $k_{||}$ point. As the slab thickness increases, the number of these hybridized bands grows and their envelope progressively approaches the smooth dispersion observed in ARPES, as demonstrated by our 41-layer versus 81-layer comparison (Figure S3). This densification reflects the scaling $\Delta E \propto 1/L_z$ along the out-of-plane direction, which governs the spacing of the discretized k_z levels. In the ideal semi-infinite crystal limit, $L_z \to \infty$, these levels would fully coalesce into a continuous bulk envelope, explaining why ARPES measurements showed a single, continuous bright feature in the projected bulk continuum, whereas finite-slab DFT calculations resolve a discrete multi-band structure.

Based on the above physical insights, we classify the SL states into absolute surface states (single, continuous bands confined within the projected band gap) and sharp surface resonances (SL states inside the bulk continuum arising from hybridization between surface-derived and bulk Bloch states).

4.2. Quantitative Characteristics of R and L

We calculated the average values of R and L (denoted as $\overline{R}$ and $\overline{L}$, respectively) for SL state features S_1–S_5 to quantify the two localization criteria. Their values show clear trends closely correlated with the intrinsic physical properties of each state.

As a typical absolute surface state in a wide band gap, S_1 exhibits negligible bulk penetration and yields high $\overline{R}$ (0.91) and $\overline{L}$ (0.81). In contrast to S_1, which resides near the gap center, S_2 lies close to the band edge of a narrow gap. This proximity enhances its bulk leakage, reducing $\overline{R}$ to 0.70 and $\overline{L}$ to 0.46. This reduced localization is consistent with the much weaker ARPES signal of S_2 relative to S_1 observed by Liang et al. [24].

Notably, the sharp surface resonance S_3 exhibits strong surface confinement within the bulk continuum, with $\overline{R}$ = 0.92 and $\overline{L}$ = 0.81—nearly equivalent to S_1—proving that spatial localization magnitude cannot reliably differentiate absolute surface states from sharp surface resonances merely via R and L thresholds. The slightly higher localization of S_3 compared with S_1 may appear counterintuitive at first glance, as S_1 is an absolute surface state confined within a band gap while S_3 is a resonance embedded in the bulk continuum. This behavior can be understood by noting that the resonance state involves hybridization between surface-originated wavefunctions and bulk Bloch states. In the case of S_3, this hybridization leads to constructive interference in the surface region and enhances the local wavefunction amplitude at the surface. The R and L criteria, which integrate the wavefunction density over the surface region, thus reflect this enhanced surface charge, resulting in values comparable to or even slightly higher than those of the gap state S_1.

The paired resonances S_4 and S_5 show asymmetric localization: S_4 ($\overline{R}$ = 0.87, $\overline{L}$ = 0.70) has marginally higher values than S_5 ($\overline{R}$ = 0.85, $\overline{L}$ = 0.69), indicative of weaker bulk hybridization, which may originate from symmetry protection or directional differences in the local bulk density of states. The larger $\overline{R}$ and $\overline{L}$ values of S_3 relative to S_5 are consistent with Hummel and Bross's theoretical conclusion that S_3 presents a sharper profile than S_5 [55]. Orbital-projection analysis reveals that S_4 exhibits a higher p_z orbital contribution (~46%) compared with S_5 (~39%), while the in-plane p_x/p_y orbital weights display the inverse trend. The enhanced p_z component strengthens the wavefunction confinement along the surface normal, suppressing in-plane hybridization with bulk states and resulting in stronger surface localization. This is consistent with the slightly higher R and L values of S_4 relative to S_5, providing a concrete orbital basis for the observed asymmetry.

To assess the sensitivity of the L criterion to the choice of λ, we performed additional calculations using λ = 4.5 Å, 10.0 Å, and 50.0 Å, alongside the NIST value of 3.17 Å employed in our main analysis. These values cover the typical kinetic energy range of photoelectrons in ARPES experiments (approximately 5–100 eV), with 4.5 Å, 3.17 Å, 10.0 Å, and 50.0 Å corresponding roughly to 100 eV (or 25 eV), 50 eV, 16 eV (or 363 eV), and 5 eV, respectively [61]. As shown in Supplementary Figure S1, although the bulk-state population shifts toward higher L values with increasing λ—consistent with the bulk bands becoming brighter in the color-coded band structures (Supplementary Figure S2)—the SL states consistently form a distinct high-value cluster around $L \approx 0.9$, while bulk states remain confined to the lower-value region. Consequently, the threshold of $L \approx 0.7$ for distinguishing SL states from bulk bands remains essentially unchanged across the tested λ range. This robustness confirms that the L criterion provides a stable and physically meaningful discrimination of SL states over typical ARPES probe depths. It is also worth noting that no explicit threshold needs to be specified when plotting the color-coded band structures; the SL states stand out clearly under the full heatmap scale (Figures 3 and S2), owing to the natural separation between the high-L SL cluster and the low-L bulk population (Figures 2 and S1).

4.3. Physical Nature of the Dual-Criterion System

The dual-criterion system is rooted in the intrinsic spatial characteristics of SL states that arise from broken translational symmetry at the surface. The surface ratio R quantifies the charge proportion confined within the full surface decay region, serving as a direct measure of the degree of localization: higher R values indicate stronger confinement and greater distinction from bulk states. The localization integral L incorporates IMFP-based exponential weighting, which naturally aligns with the surface-sensitive detection mechanism of ARPES. Either R or L alone can distinguish SL states from bulk states, but together they provide complementary decay information that enables mutual cross-verification and enhances the reliability of SL-state identification.

4.4. Advantages of the Dual-Criterion System over Traditional Methods

Our approach offers three key advantages. First, unlike gap-inspection or wavefunction matching techniques, our dual-criterion system provides automated and quantitative SL-state identification without requiring prior knowledge of band gaps or numerically delicate operations. Second, it enables the identification and quantitative characterization of the "band-to-band relay" mechanism underlying continuum surface resonances. Third, the IMFP-weighted L criterion directly links the calculation to ARPES surface sensitivity, enabling a more direct connection between computed and experimental features. Together, these advances establish our scheme as a conceptually transferable identification tool rather than a system-specific prescription.

The proposed dual-criterion framework overcomes the limitations of traditional methods, especially for weakly localized SL states. For instance, the criterion proposed by Gay et al. [37] requires 80% probability density within the outermost two atomic layers and works well for surfaces with strongly localized states like Cu(100) but fails for Al(001), whose maximum two-layer surface charge fraction only reaches 48%. Restricting integration to the top two layers leads to indistinguishable localization values between Al(001) surface states and bulk states. By contrast, our system defines the surface region as the largest decay depth of the absolute surface state, quantifies it via the surface ratio R, and introduces the IMFP-weighted localization integral L as a complementary global measure of intrinsic localization. Together, these two criteria enable reliable identification of weakly localized SL states. For new surfaces containing SL states, the largest decay depth is initially unknown and can be determined iteratively: starting from a reasonable initial guess, one identifies candidate SL states, extracts their decay depths, and refines the surface region accordingly, with convergence achieved when the change in the R values of all candidate SL states between two successive iterations falls below a specified tolerance (e.g., 1%). The choice of the convergence tolerance is based on the statistical distribution of R values (Figure 2a), where the SL and bulk populations are separated by a clear gap of approximately 0.1 in absolute R value—with bulk states clustering below $R \approx 0.5$ and SL states above $R \approx 0.6$. A tolerance of 1% (i.e., 0.01) is thus an order of magnitude smaller than this gap, ensuring stable convergence without risk of misclassification while maintaining computational efficiency.

The self-consistent iterative procedure described above is summarized as pseudocode provided in Algorithm S1 (Supplementary Information). This step-by-step implementation is intended to facilitate the application of our dual-criterion system to new material systems.

Notably, although we employ an exponential fit to extract the decay depth ℓ for Al(001) because the profiles are well described by this form (Section 3.1), the iterative procedure itself does not prescribe a specific extraction method. For systems with non-exponential or irregular decay, ℓ can be read directly from the numerical wavefunction envelope (e.g., the $1/e$ decay distance) without fitting. Moreover, n can be expressed in spatial distance (Å)

rather than in terms of the number of atomic layers, naturally accommodating complex or non-layered structures. Furthermore, the localization integral L provides an independent cross-validation: its IMFP-based exponential weight is applied globally and does not depend on n, ensuring robustness even when the decay profile deviates from a simple exponential form. This flexibility ensures that the dual-criterion system can, in principle, be applied to other surface systems, beyond the specific case of Al(001).

Unlike the mathematically intricate wavefunction matching techniques, which involve complex band structures and numerically delicate matrix operations [55,56,62,63], our dual-criterion system provides a straightforward post-processing alternative. Operating on standard DFT slab calculations, it computes two scalar indicators from the wavefunction probability density: the surface ratio R and the IMFP-weighted localization integral L. This approach avoids numerical instability, works with any standard DFT code, and directly connects to ARPES through the IMFP weighting. Together, the two indicators offer complementary validation, enabling reliable and practical identification of weakly localized surface states.

It is also worth noting that the dual-criterion framework is not specific to Al(001). The definitions of R and L depend only on the wavefunction probability density and the IMFP. The former is obtained from standard DFT slab calculations, while the latter is available from established databases (e.g., the NIST Electron Inelastic Mean Free Path Database). The choice of Al(001) as the test case is motivated by its challenging nature—its surface states exhibit exceptionally long decay depths and weak localization, representing a worst-case scenario for traditional layer-threshold criteria. The demonstration of the method on this demanding system thus provides an encouraging indication of its applicability to other surfaces where SL states are more strongly confined, such as noble metal (111) surfaces, topological insulators, and two-dimensional materials. The method is therefore proposed as a conceptually transferable framework for SL-state identification rather than a system-specific recipe.

4.5. Limitations and Future Work

Although spin–orbit coupling (SOC) is negligible for Al, our dual-criterion system is based entirely on the real-space wavefunction density and is therefore independent of spin. In principle, it can be extended to heavy-element systems (e.g., topological insulators, heavy metal surfaces) by simply including SOC in the DFT calculation. Nevertheless, all quantitative validations in this study are limited to the Al(001) surface, and two limitations of the present work merit discussion.

First, our DFT analysis does not incorporate ARPES selection-rule effects, such as photon polarization and dipole matrix elements. These factors strongly modulate photoemission intensities and can significantly alter the relative visibility of surface and bulk features, which precludes us from making a direct quantitative comparison between our calculated band structure and experimental ARPES intensities. Second, our current framework lacks the capability to systematically classify state types based on symmetry mismatch—specifically, to distinguish absolute surface states, symmetry-protected relative surface states, and hybridized surface resonances.

The present work focuses solely on wavefunction-localization-based state classification; extensions discussed below are beyond its current scope. The above-mentioned limitations suggest two clear directions for future work. First, subsequent work could introduce photoemission matrix-element simulations to account for polarization and dipole selection rules, enabling a more rigorous quantitative comparison with ARPES spectral weight distributions. Second, future work may develop a symmetry-based classification algorithm that determines the nature of each eigenstate directly from its irreducible representation, thereby

providing a fully symmetry-driven criterion to separate surface-localized states from bulk-propagating counterparts. Future work will also involve extensive validation of the proposed framework on a broad range of surfaces and low-dimensional systems—including noble-metal surfaces, topological insulator surfaces, and two-dimensional materials—to systematically characterize its full range of applicability and intrinsic limitations.

5. Conclusions

We propose a dual-criterion scheme (surface ratio R and IMFP-weighted localization integral L) to identify surface-localized (SL) states in Al(001). Applied to a fully converged 81-layer Al(001) slab, the method reveals that SL states exhibit $R > 0.7$ and $L > 0.65$, forming a clear numerical gap from bulk states ($R < 0.5$, $L < 0.25$). Five SL features are successfully identified, including the S_1 absolute surface state with a decay depth of 10.4 Å at $\overline{\Gamma}$ and the S_3 sharp resonance with a surface ratio R of 0.92. Band structures color-coded by R and L enable ARPES-like visual separation of SL and bulk states, with dispersions that agree well with experimental data. Continuum SL features arise as sharp resonances via a band-to-band relay mechanism, distinct from gap-confined absolute states.

The dual-criterion system provides a conceptually transferable framework for SL-state identification, as R and L depend only on the wavefunction density and the IMFP. The method can thus in principle be applied to other surfaces, offering a useful post-processing tool for DFT-based SL-state identification.

Supplementary Materials: The following supporting information can be downloaded at: https://www.mdpi.com/article/10.3390/cryst16080530/s1. Figure S1: Statistical histograms of the localization integral L calculated for IMFPs of (a) 3.17 Å, (b) 4.5 Å, (c) 10.0 Å, and (d) 50.0 Å; Figure S2: Band structures color-coded by the localization integral L obtained for four different inelastic mean free path (IMFP) values: (a) 3.17 Å, (b) 4.5 Å, (c) 10.0 Å, and (d) 50.0 Å; Figure S3: Band structures color-coded by the surface ratio R for (a) the 41-layer and (b) the 81-layer Al(001) slabs; Algorithm S1: Iterative determination of the surface-region parameter n; Table S1: Convergence of the surface-state energy splitting at the $\overline{\Gamma}$ point with respect to the number of atomic layers in the Al(001) slab.

Author Contributions: Conceptualization, D.-A.L.; methodology, D.-A.L.; software, X.L.; validation, D.-A.L. and X.L.; formal analysis, D.-A.L. and X.L.; investigation, D.-A.L. and X.L.; resources, X.L.; data curation, X.L.; writing—original draft preparation, X.L.; writing—review and editing, D.-A.L. and X.L.; visualization, X.L.; supervision, D.-A.L.; project administration, X.L.; funding acquisition, X.L. All authors have read and agreed to the published version of the manuscript.

Funding: This research was funded by the startup program of Guangzhou Maritime University (K42025012).

Data Availability Statement: Data are contained within the article.

Acknowledgments: The work was carried out at LvLiang Cloud Computing Center of China, and the calculations were performed on TianHe-2 supercomputer (National University of Defense Technology, Changsha, China).

Conflicts of Interest: The authors declare no conflicts of interest.

Abbreviations

The following abbreviations are used in this manuscript:

SL	Surface-localized
DFT	Density functional theory
ARPES	Angle-resolved photoemission spectroscopy

References

1. Li, D.; Bertelsen, J.L.; Papior, N.; Smogunov, A.; Brandbyge, M. Surface States and Related Quantum Interference in Ab Initio Electron Transport. *Phys. Rev. Res.* **2021**, *3*, 033017. [CrossRef]
2. Zheng, M.M.; Ren, T.Q.; Chen, G.; Kawazoe, Y. Improved Interaction of Hydrogen on Transition-Metal-Doped Al(100) Stepped Surface. *J. Phys. Chem. C* **2014**, *118*, 7442–7450. [CrossRef]
3. Chulkov, E.V.; Borisov, A.G.; Gauyacq, J.P.; Sánchez-Portal, D.; Silkin, V.M.; Zhukov, V.P.; Echenique, P.M. Electronic Excitations in Metals and at Metal Surfaces. *Chem. Rev.* **2006**, *106*, 4160–4206. [CrossRef] [PubMed]
4. Tarasov, A.V.; Estyunin, D.A.; Rybkin, A.G.; Frolov, A.S.; Sergeev, A.I.; Eryzhenkov, A.V.; Anferova, V.V.; Estyunina, T.P.; Glazkova, D.A.; Kokh, K.A.; et al. Probing the Interaction between Topological and Rashba-like Surface States in MnBi2Te4 through Sn Doping. *Phys. Rev. B* **2025**, *111*, 165115. [CrossRef]
5. Ma, X.; Wang, G.; Liu, R.; Yu, T.; Peng, Y.; Zheng, P.; Yin, Z. Correlation-Corrected Band Topology and Topological Surface States in Iron-Based Superconductors. *Phys. Rev. B* **2022**, *106*, 115114. [CrossRef]
6. Batabyal, R.; Zelzer, S.; Romagosa, A.P.; Dardzinski, D.; Corsetti, F.; Marom, N.; Krogstrup, P. Origin of Surface and Subband States at the InAs(111)A Surface. *Phys. Rev. Mater.* **2023**, *7*, 066201. [CrossRef]
7. Damascelli, A. Probing the Electronic Structure of Complex Systems by ARPES. *Phys. Scr.* **2004**, *T109*, 61. [CrossRef]
8. Lv, B.; Qian, T.; Ding, H. Angle-Resolved Photoemission Spectroscopy and Its Application to Topological Materials. *Nat. Rev. Phys.* **2019**, *1*, 609–626. [CrossRef]
9. Yang, J.; Huang, J.; Zhao, L.; Zhou, X.J. Angle-Resolved Photoemission Spectroscopy Study on Transition-Metal Kagome Materials. *Chin. Phys. B* **2025**, *34*, 047101. [CrossRef]
10. Mo, S.-K. Angle-Resolved Photoemission Spectroscopy for the Study of Two-Dimensional Materials. *Nano Converg.* **2017**, *4*, 6. [CrossRef]
11. Sobota, J.A.; He, Y.; Shen, Z.-X. Angle-Resolved Photoemission Studies of Quantum Materials. *Rev. Mod. Phys.* **2021**, *93*, 025006. [CrossRef]
12. Damascelli, A.; Hussain, Z.; Shen, Z.-X. Angle-Resolved Photoemission Studies of the Cuprate Superconductors. *Rev. Mod. Phys.* **2003**, *75*, 473–541. [CrossRef]
13. Zhang, H.; Pincelli, T.; Jozwiak, C.; Kondo, T.; Ernstorfer, R.; Sato, T.; Zhou, S. Angle-Resolved Photoemission Spectroscopy. *Nat. Rev. Methods Primers* **2022**, *2*, 54. [CrossRef]
14. Cao, Y.; Waugh, J.A.; Zhang, X.-W.; Luo, J.-W.; Wang, Q.; Reber, T.J.; Mo, S.K.; Xu, Z.; Yang, A.; Schneeloch, J.; et al. Mapping the Orbital Wavefunction of the Surface States in Three-Dimensional Topological Insulators. *Nat. Phys.* **2013**, *9*, 499–504. [CrossRef]
15. Kemper, A.F.; Goto, F.; Labib, H.A.; Gauthier, N.; Neto, E.H.D.S.; Boschini, F. Observing Two-Electron Interactions with Correlation-ARPES. *Phys. Rev. B* **2025**, *112*, 035168. [CrossRef]
16. Kuibarov, A.; Suvorov, O.; Vocaturo, R.; Fedorov, A.; Lou, R.; Merkwitz, L.; Voroshnin, V.; Facio, J.I.; Koepernik, K.; Yaresko, A.; et al. Evidence of Superconducting Fermi Arcs. *Nature* **2024**, *626*, 294–299. [CrossRef] [PubMed]
17. Gao, Q.; Bok, J.M.; Ai, P.; Liu, J.; Yan, H.; Luo, X.; Cai, Y.; Li, C.; Wang, Y.; Yin, C.; et al. ARPES Detection of Superconducting Gap Sign in Unconventional Superconductors. *Nat. Commun.* **2024**, *15*, 4538. [CrossRef] [PubMed]
18. Khaled, M.A.; Cancellara, L.; Fekraoui, S.; Daubriac, R.; Bertran, F.; Bigi, C.; Gravelier, Q.; Monflier, R.; Arnoult, A.; Durand, C.; et al. Large-Scale Epitaxial Integration of Single-Crystalline BiSb Topological Insulator on GaAs (111)A. *ACS Appl. Electron. Mater.* **2024**, *6*, 3771–3779. [CrossRef]
19. Nguyen, K.D.; Berruto, G.; Lee, S.H.; Bai, Y.; Lin, H.; Gao, Q.; Mao, Z.; Yang, S. Spectroscopic Evidence of Intra-Unit-Cell Charge Redistribution in a Charge-Neutral Magnetic Topological Insulator. *Nanoscale* **2025**, *17*, 10663–10669. [CrossRef] [PubMed]
20. Boschini, F.; Zonno, M.; Damascelli, A. Time-Resolved ARPES Studies of Quantum Materials. *Rev. Mod. Phys.* **2024**, *96*, 015003. [CrossRef]
21. Sunko, V. *Angle Resolved Photoemission Spectroscopy of Delafossite Metals*; Springer Theses; Springer International Publishing: Cham, Germany, 2019.
22. Wang, E. *Angle-Resolved Photoemission Spectroscopy Studies of 2D Material Heterostructures*; Springer Theses; Springer: Singapore, 2020.
23. Reinert, F.; Nicolay, G.; Schmidt, S.; Ehm, D.; Hüfner, S. Direct Measurements of the *L* -Gap Surface States on the (111) Face of Noble Metals by Photoelectron Spectroscopy. *Phys. Rev. B* **2001**, *63*, 115415. [CrossRef]
24. Liang, X.; Cheng, C.-M.; Tsuei, K.-D.; Luh, D.-A. Surface Band Structure of Al(100) Studied with High-Resolution Angle-Resolved Photoelectron Spectroscopy. *J. Electron Spectrosc. Relat. Phenom.* **2012**, *184*, 551–555. [CrossRef]
25. Hansson, G.V.; Flodström, S.A. Photoemission from Surface States and Surface Resonances on the (100), (110), and (111) Crystal Faces of Aluminum. *Phys. Rev. B* **1978**, *18*, 1562–1571. [CrossRef]
26. Bentouaf, A.; Hassan, F.H.; Reshak, A.H.; Aïssa, B. First-Principles Study on the Structural, Electronic, Magnetic and Thermodynamic Properties of Full Heusler Alloys Co2VZ (Z = Al, Ga). *J. Electron. Mater.* **2017**, *46*, 130–142. [CrossRef]

27. Belhadj, M.E.A.; Berrahal, M.; Bentouaf, A.; Belmekki, M.; Elaissaoui El Meliani, M.E.A.; Benaddi, F.; Azzouz Rached, A. Structural Parameters, Electronic Structure, Magnetic, and Mechanical Properties of Half-Metallic Full-Heusler Compound Cr2VAs: A Density Functional Theory Study. *Comput. Theor. Chem.* **2024**, *1234*, 114526. [CrossRef]
28. Benaddi, F.; Bentouaf, A.; Rached, A.A. Structural, Electronic and Thermoelectric Properties of the RENi2 (RE = Dy, Er, Ho) Rare Earth Intermetallic Compounds: A Density-Functional-Theory Investigation. *Eur. Phys. J. B* **2025**, *98*, 139. [CrossRef]
29. Sangiovanni, D.G.; Gueorguiev, G.K.; Kakanakova-Georgieva, A. Ab Initio Molecular Dynamics of Atomic-Scale Surface Reactions: Insights into Metal Organic Chemical Vapor Deposition of AlN on Graphene. *Phys. Chem. Chem. Phys.* **2018**, *20*, 17751–17761. [CrossRef] [PubMed]
30. Bencheikh, M.; El Farh, L.; Malki, S.; Guesmi, I.; Darhi, Z.; Challioui, A. A DFT Study of the Structural, Optoelectronic, Elastic, and Thermodynamic Properties of the Tetragonal Monochalcogenide InTe. *Opt. Quant. Electron.* **2024**, *56*, 1348. [CrossRef]
31. Iram, N.; Sharma, R.; Ahmad, J.; Kumar, A.; Kumar, A.; Almutairi, F.N.; Alturaifi, H.A. A DFT Manifestation of the Physical, Thermodynamic and Thermoelectric Properties in Sn-Based Halide Perovskites. *Inorg. Chem. Commun.* **2025**, *172*, 113573. [CrossRef]
32. Xu, T.; Liu, S.; Il Seok, S.; Xiang, W. Surface Chemistry-Induced Reconstruction of Inorganic Perovskites for Efficient and Stable Inverted Solar Cells. *Joule* **2025**, *9*, 101826. [CrossRef]
33. Guan, Y.; Jiang, S.; Ding, Y.; Xiao, B.; Pi, Y.; Wang, Z.; Cong, Y. Insight into the Mechanism of Nitrogen Doping in MXenes with Controllable Surface Chemistry. *Mater. Today Energy* **2024**, *44*, 101642. [CrossRef]
34. Jiang, M.; Wang, D.; Kim, Y.; Duan, C.; Talapin, D.V.; Zhou, C. Evolution of Surface Chemistry in Two-Dimensional MXenes: From Mixed to Tunable Uniform Terminations. *Angew. Chem. Int. Ed.* **2024**, *63*, e202409480. [CrossRef] [PubMed]
35. Sammüller, F.; Schmidt, M.; Evans, R. Neural Density Functional Theory of Liquid-Gas Phase Coexistence. *Phys. Rev. X* **2025**, *15*, 011013. [CrossRef]
36. Kern, G.; Hafner, J. Ab Initio Calculations of the Atomic and Electronic Structure of Clean and Hydrogenated Diamond (110) Surfaces. *Phys. Rev. B* **1997**, *56*, 4203–4210. [CrossRef]
37. Gay, J.G.; Smith, J.R.; Arlinghaus, F.J. Large Surface-State/Surface-Resonance Density on Copper (100). *Phys. Rev. Lett.* **1979**, *42*, 332–335. [CrossRef]
38. Takeuchi, N.; Chan, C.T.; Ho, K.M. Au(111): A Theoretical Study of the Surface Reconstruction and the Surface Electronic Structure. *Phys. Rev. B* **1991**, *43*, 13899–13906. [CrossRef] [PubMed]
39. Bullett, D.W. Surface States and the Local Electronic Structure at Surfaces. *Philos. Mag. B* **1985**, *51*, 223–241. [CrossRef]
40. Da Silva, J.L.F. All-Electron First-Principles Calculations of Clean Surface Properties of Low-Miller-Index Al Surfaces. *Phys. Rev. B* **2005**, *71*, 195416. [CrossRef]
41. Knebl, D. Shockley Surface States from First Principles. Master's Thesis, Karl-Franzens-Universität Graz, Graz, Austria, 2013.
42. Heinrichsmeier, M.; Fleszar, A.; Eguiluz, A.G. LDA Calculation of the Surface States on the (001), (110), and (111) Surfaces of Aluminum. *Surf. Sci.* **1993**, *285*, 129–141. [CrossRef]
43. Sklyadneva, I.Y.; Chulkov, E.V.; Echenique, P.M. Electron–Phonon Interaction on an Al(001) Surface. *J. Phys. Condens. Matter* **2008**, *20*, 165203. [CrossRef]
44. Giannozzi, P.; Andreussi, O.; Brumme, T.; Bunau, O.; Buongiorno Nardelli, M.; Calandra, M.; Car, R.; Cavazzoni, C.; Ceresoli, D.; Cococcioni, M.; et al. Advanced Capabilities for Materials Modelling with Quantum ESPRESSO. *J. Phys. Condens. Matter* **2017**, *29*, 465901. [CrossRef] [PubMed]
45. Giannozzi, P.; Baroni, S.; Bonini, N.; Calandra, M.; Car, R.; Cavazzoni, C.; Ceresoli, D.; Chiarotti, G.L.; Cococcioni, M.; Dabo, I.; et al. QUANTUM ESPRESSO: A Modular and Open-Source Software Project for Quantum Simulations of Materials. *J. Phys. Condens. Matter* **2009**, *21*, 395502. [CrossRef] [PubMed]
46. Perdew, J.P.; Ruzsinszky, A.; Csonka, G.I.; Vydrov, O.A.; Scuseria, G.E.; Constantin, L.A.; Zhou, X.; Burke, K. Restoring the Density-Gradient Expansion for Exchange in Solids and Surfaces. *Phys. Rev. Lett.* **2008**, *100*, 136406. [CrossRef] [PubMed]
47. SSSP. Available online: https://legacy.materialscloud.org/discover/sssp (accessed on 2 May 2026).
48. Prandini, G.; Marrazzo, A.; Castelli, I.E.; Mounet, N.; Marzari, N. Precision and Efficiency in Solid-State Pseudopotential Calculations. *npj Comput. Mater.* **2018**, *4*, 72. [CrossRef]
49. Staroverov, V.N.; Scuseria, G.E.; Tao, J.; Perdew, J.P. Tests of a Ladder of Density Functionals for Bulk Solids and Surfaces. *Phys. Rev. B* **2004**, *69*, 075102. [CrossRef]
50. Sferco, S.J.; Blaha, P.; Schwarz, K. Deep Multilayer Relaxations on the Al(001) Surface: Ab Initio All-Electron Calculations. *Phys. Rev. B* **2007**, *76*, 075428. [CrossRef]
51. Jorgensen, J.J.; Hart, G.L.W. Effectiveness of Smearing and Tetrahedron Methods: Best Practices in DFT Codes. *Model. Simul. Mater. Sci. Eng.* **2021**, *29*, 065014. [CrossRef]
52. Hjorth Larsen, A.; Jørgen Mortensen, J.; Blomqvist, J.; Castelli, I.E.; Christensen, R.; Dułak, M.; Friis, J.; Groves, M.N.; Hammer, B.; Hargus, C.; et al. The Atomic Simulation Environment—A Python Library for Working with Atoms. *J. Phys. Condens. Matter* **2017**, *29*, 273002. [CrossRef] [PubMed]

53. Veusz—A Scientific Plotting Package. Available online: https://veusz.github.io/ (accessed on 2 May 2026).
54. Powell, C.J.; Jablonski, A. *NIST Electron Inelastic-Mean-Free-Path Database, Version 1.2.*; National Institute of Standards and Technology: Gaithersburg, MD, USA, 2010.
55. Hummel, W.; Bross, H. Determining the Electronic Properties of Semi-Infinite Crystals. *Phys. Rev. B* **1998**, *58*, 1620–1632. [CrossRef]
56. Wachutka, G. New Layer Method for the Investigation of the Electronic Properties of Two-Dimensional Periodic Spatial Structures: First Applications to Copper and Aluminum. *Phys. Rev. B* **1986**, *34*, 8512–8527. [CrossRef] [PubMed]
57. Levinson, H.J.; Greuter, F.; Plummer, E.W. Experimental Band Structure of Aluminum. *Phys. Rev. B* **1983**, *27*, 727. [CrossRef]
58. Chulkov, E.V.; Silkin, V.M. Electronic Structure of the Al(001) Surface with Adsorbed Na Halfmonolayer. *Surf. Sci.* **1989**, *215*, 385–393. [CrossRef]
59. Gartland, P.O.; Slagsvold, B.J. Angular Resolved Photoemission from Intrinsic Surface States on Al(100). *Solid State Commun.* **1978**, *25*, 489–492. [CrossRef]
60. Caruthers, E.; Kleinman, L.; Alldredge, G.P. Energy Bands for the (001) Surface of Aluminum. *Phys. Rev. B* **1973**, *8*, 4570–4577. [CrossRef]
61. De Vera, P.; Garcia-Molina, R. Electron Inelastic Mean Free Paths in Condensed Matter Down to a Few Electronvolts. *J. Phys. Chem. C* **2019**, *123*, 2075–2083. [CrossRef]
62. Appelbaum, J.A.; Hamann, D.R. Self-Consistent Electronic Structure of Solid Surfaces. *Phys. Rev. B* **1972**, *6*, 2166–2177. [CrossRef]
63. Jepsen, D.W. New Transfer-Matrix Method for Low-Energy-Electron Diffraction and Other Surface Electronic-Structure Problems. *Phys. Rev. B* **1980**, *22*, 5701–5715. [CrossRef]